JEMMME (Journal of Energy, Mechanical, Material, and Manufacturing Engineering)
Vol. 8, No. 2, 2023

ISSN 2541-6332 | e-ISSN 2548-4281
Journal homepage: http://ejournal.umm.ac.id/index.php/JEMMME

Effects of leading-edge defects of the NACA 0015 airfoil on aerodynamic performance with various Reynolds number

Ulfa Hanifah Nurhaliza[a], James Julian[a], Fitri Wahyuni[a], Waridho Iskandar[b]
[a] Mechanical Engineering, Universitas Pembangunan Nasional Veteran Jakarta
Jl. R.S. Fatmawati No.1, Jakarta Selatan 12450, DKI Jakarta, Indonesia
+62 765 6971

[b] Fluid Mechanics Laboratory, University Indonesia
Kampus Baru UI, Depok 16424, Jawa Barat, Indonesia
+62 21 786 7222
e-mail: ulfa.hanifahn@upnvj.ac.id, zames@upnvj.ac.id, fitriwahyuni@upnvj.ac.id, waridho.iskandar@ui.ac.id

Abstract

This study investigates and identifies the effects produced by defect on an airfoil when compared to a smooth airfoil. The defect used in this research is one form of the surface concaved defect (SDD) type deformation because it can represent the serious damage caused by severe impact or erosion and the deep defect characterized by a smooth sunken deformation. The opening size used is t^*=12%, and the equivalent depth of the defect is h=3%. Computational methods are being used in this research to analyzing flow of the fluid through the NACA 0015 airfoil, both in smooth and defective airfoil, with various Reynolds Number which are 1.6×10^6, 2×10^6, and 2.5×10^6. Standard k-epsilon model is being used in this research as turbulence model. For the smooth airfoil, stall conditions occur at an AoA of 11º, while for the defective airfoil, they occur at an AoA of 9^° for each Re variation. The average decrease in the C_l/C_d ratio from smooth airfoil to defective airfoil at each AoA for all Re variations is 33%. Based on the velocity streamlines, vortices can be found at the defect cavity, and the vortex at the defective airfoil seems larger than the smooth airfoil.*

Keywords: *NACA 0015; CFD Simulation; Reynolds Number; Defect Airfoil; Aerodynamic Forces*

1. INTRODUCTION

Fossil fuels are depleted as alternative development of the energy resources has become more essential. On the other hand, the world has become engulfed by a global energy crisis, and leads to rapid increase in demand for energy worldwide (1). The existence of renewable and sustainable energy is crucial at this moment, in other words it is urgently needed. It is necessary for the world to have energy that can be used efficiently and effectively, without reducing the world required energy consumption. Hence, increasing the use of wind energy as the renewable energy sources has become a solution to meet the world's energy needs. One of the methods for harnessing wind energy is through wind turbines. Wind turbines have become essential in the process of converting wind energy into electrical energy. During this process, the rotation of wind turbine blades occurs at high speeds and is exposed to various weather conditions such as rain, sunlight, snow, and ultraviolet rays. Typically, wind turbine blades are coated to protect them from erosion caused by rain. Rain-induced erosion poses a mechanical threat to the integrity of the turbine blades (2). Besides rain, airborne sand particles can also have a detrimental impact on the rotating wind turbine blade surfaces, causing erosion (3). Small shallow pits that form at the leading edge of the airfoil are typically the

first signs of erosion. Over time, these pits grow and converge to form surface irregularities. Impact on the aerodynamic behaviour of blades can be caused by defects in the leading edge of the airfoil, which makes large-scale wind turbines significantly has loss of its power efficiency (4). Surface concaved deep defects (SDD) in the leading-edge airfoil, which show severe damage brought on by heavy erosion, and surface distributed shallow defects (SSD) in the leading-edge airfoil, which appear on the blade's surface layer due to light erosion, are the two types that can be categorized based on the geometric leading-edge defect characteristics (5).

The effects of defects on the leading-edge airfoil have been the subject of numerous studies. Wang et al. studied the size and equivalent depth of rectangular-shaped defect effects, demonstrating that for SDD on the leading edge, when h/t>0.5, the size of the defect has a major impact on the aerodynamic performance of the airfoil, and defects can cause flow separation at the trailing edge and the formation of bubbling circulation in the defect cavity (6). Sareen et al. investigated the effects of SSD using tunnel tests. The effects that being investigated are shallow holes, gouges, and delamination. The results showed that there is highly increased of the drag coefficient that strongly affected by the roughness or degree of leading-edge defects. In their case, all drag increased by more than 6% (7). Ge et al. studied different defects on the leading-edge airfoil S809 with varying defect shapes, spans, and equivalent depths, and investigated them using CFD. The findings demonstrated that while the defect shape and equivalent depth can only slightly affect the airfoil's aerodynamic performance, the defect's span can exhibit high sensitivity (8).

Regarding the effect of leading-edge defects on an airfoil, the aforementioned research has produced a number of conclusions. Numerous studies have concentrated on various defect geometries with important factors like defect span, shape, and equivalent depth on the airfoil. However, in reality, understanding the effects of flow phenomena around the airfoil cannot be separated from the flow velocity. Therefore, this research offers a different perspective on examining the impact of leading-edge defects on an airfoil by considering the influence of changes in the Reynolds Number due to varying wind speeds on airfoil performance. This is supported by the actual conditions of wind turbine usage, which do not always operate at a constant wind speed.

2. METHODS

2.1 Reynolds Number

The Reynolds number is a dimensionless parameter, and its influence is intricately linked to the notion of dynamic similarity when comparing turbulent and laminar flows [8]. The Reynolds number serves as a means to measure the significance of inertia effects, which relate to fluid momentum, in relation to viscous effects, representing fluid stickiness, in determining the behavior of an airfoil (9). The drag and lift coefficients of the airfoil can experience considerable modifications due to varieties within the Angle of Attack (AoA) and the Reynolds number. These changes are influenced by the airfoil's geometry in relation to the direction of incoming fluid flow. The formula for determining the Reynolds number, denoted as Re, can be expressed as illustrated in Equation 1. Here, ρ denotes the density of the fluid, V signifies the speed of the stream, c stands for the characteristic dimension of the object under consideration which in this study, it corresponds to the chord length, and μ represents the coefficient of dynamic viscosity.

$$Re = \frac{\rho V c}{\mu} \tag{1}$$

2.2 Geometry Model

The design of a particular airfoil type, such as the NACA 0015 airfoil, was carried out by the National Advisory Committee for Aeronautics (NACA). The NACA 0015 airfoil falls into the class of symmetrical airfoils (10). The code "0015" carries a specific meaning: the presence of zeroes in the first and second positions indicates the absence of camber in this airfoil. The analysis of third and fourth digits, representing 15% of the chord's length,

may be used to determine the outermost thickness of an airfoil. In Figure 1, the length of the chord is denoted as "c," and in this investigation, a chord length of 1 meter is adopted. Additionally, this study involves the modification of the NACA 0015 airfoil by introducing defects on its surface, specifically, concave defects referred to as Surface Concaved Defects (SDD). These defects are characterized by deep depressions that create smooth, sunken deformations. The primary parameters under consideration in this research encompass the aperture size, expressed as $t^*=t/t_a$ =12%, and the corresponding depth of the defect, denoted as $h^*=h/c$=3%. It's worth noting that these values are determined in relation to t_a as the airfoil's maximum thickness, and it's the length of the chord, denoted as c, to quantify the size and depth of a specific defect. Figure 2 illustrates the altered shape of the NACA 0015 airfoil as per the applied defect parameters.

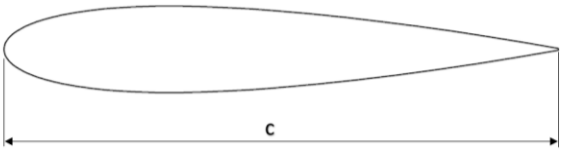

Figure 1. NACA 0015

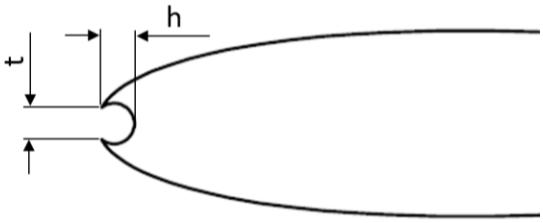

Figure 2. NACA 0015 *SDD*

2.3 Numerical Method

In this study, the mathematical framework utilized is the Reynolds Averaged Navier Stokes (RANS) model, which composed by two core equations: both the momentum equation and the continuity equation. These particular RANS equations, as detailed in equations 2 and 3 (11), serve different functions. Equation 2 deals with the consistency of fluid movement, whereas equation 3 focuses on changes in the momentum of fluid flow. It's crucial to emphasize that in this analysis, we assume that fluid flow takes place only in the x-axis direction.

$$\frac{\partial \rho}{\partial t} + \frac{\partial}{\partial x_i}(\rho u_i) = 0 \tag{2}$$

$$\frac{\partial}{\partial t}(\rho u_i) + \frac{\partial}{\partial x_i}(\rho u_i u_j) = \frac{\partial \rho}{\partial x_i} + \frac{\partial}{\partial x_j}\left[\mu\left(\frac{\partial u_i}{\partial x_j} + \frac{\partial u_j}{\partial x_i} - \frac{2}{3}\delta_{ij}\frac{\partial u_i}{\partial x_i}\right)\right] + \frac{\partial}{\partial x_i}\left(\rho\overline{u_i'}u_j'\right) \tag{3}$$

In this investigation, we use the accepted k-ε turbulence model as an extension to enhance the RANS equations. Two equations make up the k-ε turbulence model: one for the flow of turbulent kinetic energy (k) and another for the rate of turbulent dissipation (ε) (12). Spalding and Launder were the pioneers in the initial creation of the k-ε turbulence model. This particular turbulence model stands out as a widely favored choice in CFD analysis due to its cost-effectiveness per iteration. Furthermore, it proves highly

adaptable for modeling various fluid flow scenarios, both internal and external. Equations (4) and (5) contain the standard equations for the k-ε turbulence model (13).

$$\frac{D}{D_t}(\rho k) = \frac{\partial}{\partial x_j}\left[\left(\mu + \frac{\mu_t}{\sigma_k}\right)\frac{\partial k}{\partial x_j}\right] + G_k - \rho\varepsilon \tag{4}$$

$$\frac{D}{D_t}(\rho \varepsilon) = \frac{\partial}{\partial x_j}\left[\left(\mu + \frac{\mu_t}{\sigma_\varepsilon}\right)\frac{\partial \varepsilon}{\partial x_j}\right] + C_{\varepsilon 1}\frac{\varepsilon}{k}G_k - \rho C_{\varepsilon 2}\frac{\varepsilon^2}{k} \tag{5}$$

Where $C_{\varepsilon 2} = 1.92, \sigma_\varepsilon = 1.3, C_\mu = 0.09, C_{\varepsilon 1} = 1.44$

2.4 Domain, Mesh, and Boundary Conditions

To lessen the influence of boundary positions on the results of the computation, the domain's dimensions have been carefully selected. The airfoil's trailing edge is centered in the circular domain. An inlet velocity boundary and an outlet pressure boundary are the two boundary types that divide this domain. In order to guarantee no-slip conditions, the surface of the airfoil simultaneously can be considered as boundary which is a wall. The entire fluid flow domain and the necessary of the computational process's boundary conditions are shown in Figure 3. Variations in the AoA are achieved by adjusting the velocity components along both the X and Y directions. In this study, quadrilateral mesh elements have been employed. The primary benefit of using quadrilateral mesh elements lies in their versatility to conform to objects with curved shapes. Consequently, this type of mesh is particularly well-suited for modeling the NACA 0015 airfoil, as it possesses curved features on both its upper and lower surfaces, as depicted in Figure 4.

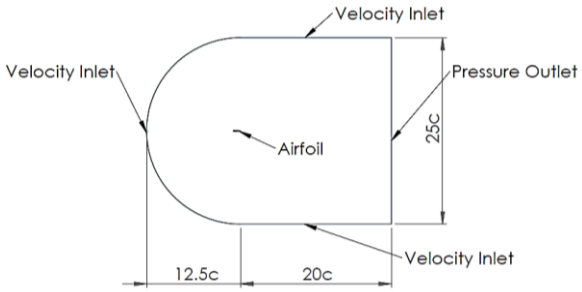

Figure 3. Computational Domain and Boundary Conditions

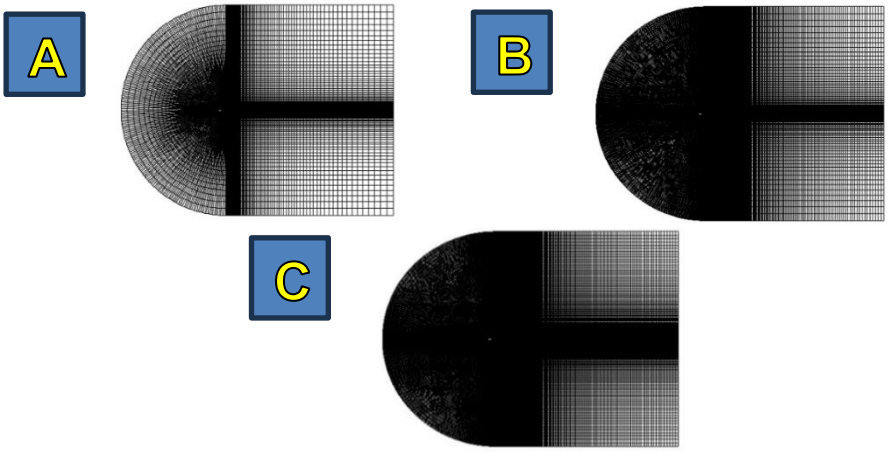

Figure 4. Mesh. (a) 25×10³ Elements; (b) 5×10⁴ Elements; and (c) 1×10⁵ Elements

2.5 Mesh Independence Study

The Richardson extrapolation method, as described by Roache, is used in this study to evaluate the mesh independence with the flow shown in Figure 5. This evaluation includes several equations that were used during the process. Utilizing Equation 6, the mesh variation ratio is first assessed by dividing grid refinement on grids of spacing h_1 and h_2, with h_1 being finer (smaller) spacing. In this study, order determination that represented by $\bar{p}$ can be governed by Equation 7, where f_1, f_2, and f_3 respectively are discrite solution for fine, medium, and coarse mesh. Then, defining the error in the mesh variation that currently has been made in this study using Grid Independence Test. To evaluate the mesh error, the Grid Convergence Index (GCI) is employed in this study with Factor of Safety, F_s =1,25. There are two specific GCI types applied in the analysis. The first one, denoted as GCI_{fine}, serves to measure the difference in error between the medium and fine meshes, as shown by Equation 8. On the other hand, the second GCI, termed GCI_{coarse}, is utilized to quantify the error between the medium and coarse meshes, as described in Equation 9. Equation 10 is employed for the calculation of the relative error ϵ. The mesh independence test serves two primary purposes. Then, using equation 11 for determining the range of the convergence so that the mesh variation that has been made can be known as a part of the convergence range. Secondly, it aims to identify the optimal number of grid points for the subsequent computational phase. The choice of the mesh relies on achieving the lowest relative error concerning a particular parameter value, which can be computed using Equation 12, where $f_{r_h=0}$ represents Richardson Extrapolation (14).

$$r = \frac{h_2}{h_1} \tag{6}$$

$$\bar{p} = \frac{ln\left(\frac{f_3 - f_2}{f_2 - f_1}\right)}{\ln(r)} \tag{7}$$

$$GCI_{fine} = \frac{F_s|\epsilon|}{(r^{\bar{p}} - 1)} \tag{8}$$

$$GCI_{coarse} = \frac{F_s|\epsilon|r^{\bar{p}}}{(r^{\bar{p}} - 1)} \tag{9}$$

$$\epsilon = \frac{f_{n+1} - f_n}{f_n} \tag{10}$$

$$\frac{GCI_{fine}}{GCI_{coarse}r^{\bar{p}}} \approx 1 \tag{11}$$

$$f_{r_h=0} = f_1 + \frac{(f_1 - f_2)}{(r^{\bar{p}} - 1)} \tag{12}$$

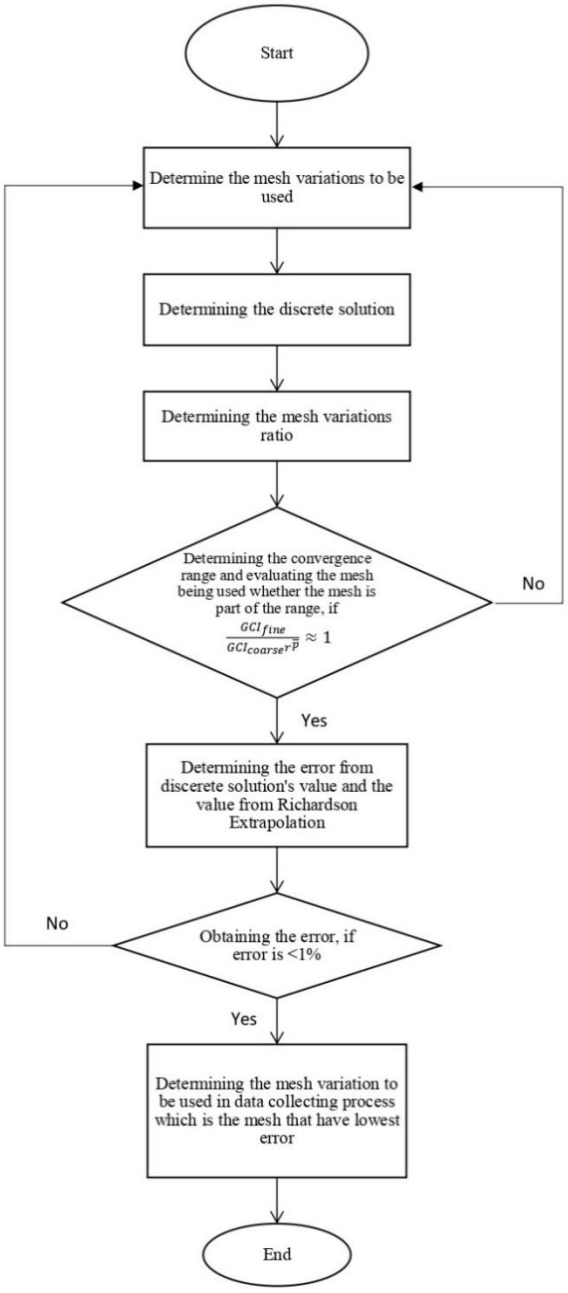

Figure 5. Grid Independence Test Flowchart

2.6 Aerodynamic Forces

Lift and drag forces are the two main aerodynamic forces generated by the airfoil. Due to the airfoil's shape, airflow is diverted over its upper surface, which causes air pressure to drop or a low-pressure area to form on the upper side, which produces the lift force. The lift forces are perpendicular to the direction of the airflow. Conversely, an airfoil is also experiencing another aerodynamic force known as drag power that works alongside the direction of airflow and acts in the opposite direction of the airfoil's motion relative to it (15). The magnitude of these aerodynamic forces is affected by various factors, including fluid velocity, airfoil surface characteristics, fluid viscosity, and the AoA of the airfoil. In this study, compressibility effects can be disregarded as the simulated fluid flow is considered incompressible. Generally, aerodynamic force coefficients are expressed in dimensionless form. The lift coefficient is commonly represented as C_l, while the drag coefficient is indicated as C_d. The equations C_l dan C_d are provided in equations 13 and 14 (16).

$$C_l = \frac{l}{\frac{1}{2}\rho V^2 c} \tag{13}$$

$$C_d = \frac{d}{\frac{1}{2}\rho V^2 c} \tag{14}$$

3. RESULT AND DISCUSSION

3.1 Mesh Independence Test

In order to check that the type of meshes which will be used in this study have been independent, an independence test shall be carried out. The mesh being evaluated has three variations as shown in Figure 4. The Reynolds number to be used in the mesh independence test is 1.6×10^6. The discrete solution applied to the fluid velocity has its coordinate points located at X=0, Y=-0.5, and Z=0.02. The mesh ratio can be calculated using Equation 6, resulting in a value of r=2. The mesh convergence order is obtained through Equation 7, which yields a value of 2.471.

Table 1. Mesh Independence Test Result

Mesh Type	Velocity (u)	Discrete Solution	Error
fine	3.99949	f_1	0.1324%
medium	3.9754	f_2	0.7339%
coarse	3.84185	f_3	4.0687%

The relative error calculated using Equation 10 results in $\epsilon=1.83\times10^4$ for GCI_{fine} and $\epsilon=1.1\times10^3$ for GCI_{coarse}. Afterward, the values of GCI_{fine} and GCI_{coarse} can be calculated using Equation 8 and 9 with a value of $F_s=1.25$. The calculation results using Equation 11 yield $\frac{GCI_{fine}}{GCI_{coarse}r^{\bar{p}}} \approx 1$. Thus, the mesh variations created can be confirmed to fall within the convergence range. To determine the mesh variation to be used, the difference between the value of the discrete solution and the value from Equation 12 is calculated, divided by the value of the discrete solution so that the error can be seen as Table 1. Therefore, the mesh with a number of elements of 1×10^5 is considered the optimal choice for this study, as it produces the smallest error compared to other variations.

3.2 Validation

Parameter validation is needed to ensure that the flow conditions during simulation closely resemble real-world conditions. Validation is conducted by comparing C_l and C_d for NACA 0015 at Reynolds Number 1.6×10^5. The comparison data for the validation process comes from experimental data obtained in a study conducted by Kekina (17). Graph 1a shows that the curve of C_l obtained from experimental results and CFD exhibits similar patterns for α≤10^°, and the C_l curve indicates conditions close to a linear curve. There is a sudden decrease in C_l value, or stall conditions occur at 12º for experimental results, while the CFD simulation results show stall at 14°. The C_d value is also affected by stall conditions, as evidenced by the extreme increase in C_d value after stall conditions occur, as shown in Graph 1b. It can be observed that when α≤10°, the C_d curve exhibits a similar pattern between experimental and CFD results. Meanwhile, for α≥10° there are inaccuracies which may be caused by deficiencies in RANS and the complex vortex structure in deep stall conditions when the flow is in a condition of large separation, besides that there are also difficulties in measuring the pressure in the layer when conducting experiments in the wind tunnel which is caused by by complex vortices.

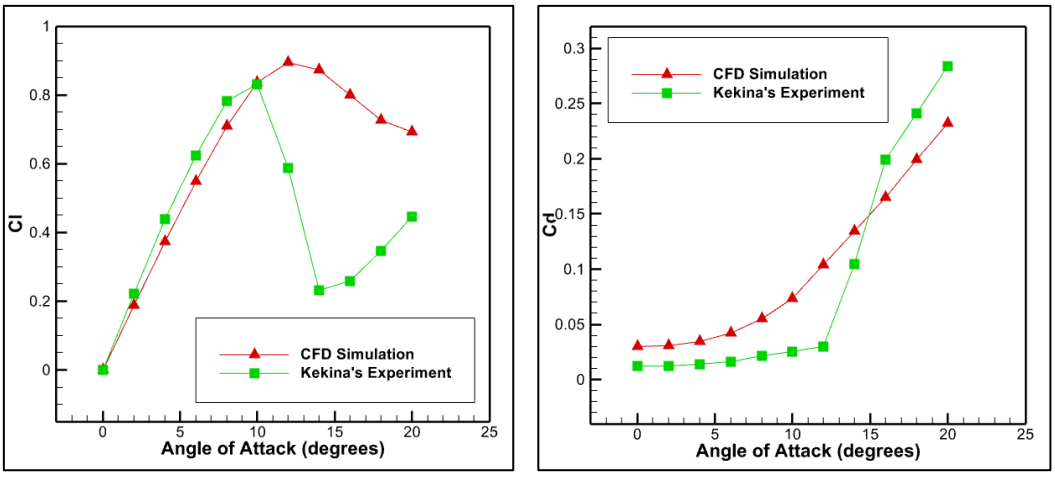

(a) C_l *(b) C_d*

Graph 1. Validation Results

3.3 Analysis of Airfoil Performance

In Graph 2, you can see the C_l and C_d curves for all angles of attack with variations in Re of 1.6×10^6, 2×10^6 and 2.5×10^6 between the smooth airfoil and the defective airfoil also you can see the CFD simulation results from research on the effect of the shape of the defect on the leading edge of the S809 airfoil on Aerodynamic Performance carried out by Mingwei Ge (5) with the shape of the smooth sunken deformation in the form of an SDD with sizes t*=12% and h*=3%. The research of S809 Airfoil was carried out in $Re=1\times10^6$ and its C_l curve shows an increase in C_l along the AoA until stall conditions for both defective airfoils and smooth airfoils. Overall, the C_l curve proves that the C_l produced by a defective airfoil is lower than that produced by a smooth airfoil. Apart from that, the C_d curve of S809 Airfoil can show the increase in C_d along the AoA until the stall condition then the increase becomes more extreme. Defects in the airfoil also cause an increase in C_d compared to the C_d produced by a smooth airfoil. Also, can be seen that the C_l/C_d ratio curve of S809 Airfoil increases along the AoA until the stall condition and the aerodynamic efficiency produced by the defective airfoil is lower when compared to the smooth airfoil. The things that already mentioned were also happened in this research of NACA 0015 Airfoil which can be seen in Graph 2.

From Graph 2a, it can be concluded that the increase in C_l is proportional to the escalating of the AoA. However, after passing a certain AoA, C_l will decrease. The AoA at which the airfoil experiences a decrease in C_l indicates that the airfoil has reached the stall condition. All Re variations for both the smooth airfoil and the defective airfoil show the same curve pattern. In the defective airfoil, stall condition take place at an AoA of 9º, whereas in the smooth airfoil, it comes about at an AoA of 11º for all Re variations. This suggests that defects in the airfoil cause the stall condition to occur earlier than in the smooth airfoil. Although stall occurs at the same AoA, C_l values increase with increasing Re. It can also be observed that the presence of defects in the airfoil can reduce C_l values across the entire extent of angles of attack compared to the smooth airfoil. The defective airfoil results in an average 44% reduction in C_l at $Re=1.6\times10^6$ compared to the smooth airfoil. Furthermore, at $Re=2\times10^6$ and $Re=2.5\times10^6$, there is an average 47% decrease in C_l values across all angles of attack.

Next, for the C_d curve, it is provided in Graph 2b. An increase in C_d occurs as the AoA rises for both the defective airfoil and the smooth airfoil. Both the defective airfoil and the smooth airfoil have the same curve pattern, and the increase in C_d values has become more extreme when entering the stall angle across all Re variations. Additionally, it can be observed that an increase in Re values also lead to an increase in C_d values. Defects in the airfoil also result in an increase in C_d values when compared to the smooth airfoil. The average increase in C_d values at each AoA is 19% at $Re=1.6\times10^6$, 24% at $Re=2\times10^6$, and 23% at $Re=2.5\times10^6$.

In Graph 2c, you can observe the curve of the C_l/C_d ratio, also known as aerodynamic efficiency. The curve patterns for the C_l/C_d ratio for both the smooth airfoil and the defective airfoil have similar patterns at each Re variation. There is an increase in the C_l/C_d ratio in line with the escalate in the AoA until the airfoil reaches stall conditions at an AoA of 9º for the defective airfoil and 11º for the smooth airfoil. After the airfoil experiences stall conditions, the C_l/C_d ratio also decreases due to the decrease in C_l values and the extreme increase in C_d values. The maximum C_l/C_d ratio is achieved at an AoA of 5º for the smooth airfoil at each Re variation, while for the defective airfoil, it reaches the maximum C_l/C_d ratio at angles of attack of 6º, 4º, and 5º respectively for Re=1.6×10^6, Re=2×10^6, and Re=2.5×10^6. The presence of defects in the airfoil also leads to a reduction in the C_l/C_d ratio compared to the smooth airfoil. This is evidenced by the average decrease in the C_l/C_d ratio at each AoA for all Re variations, which is 33%.

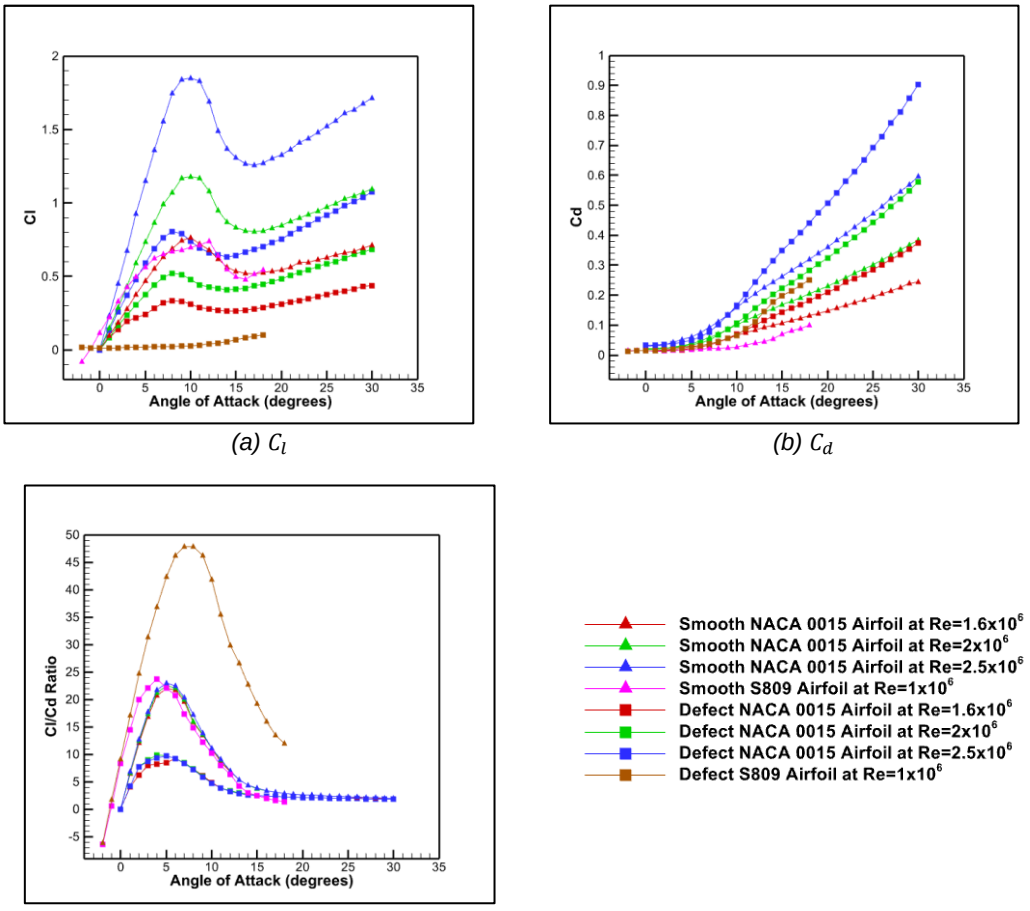

(a) C_l *(b) C_d*

(c) C_l/C_d Ratio

Graph 2. Aerodynamic Forces

3.4 Visualization of Fluid Flow Analysis

The pressure and velocity distribution around the airfoil region is illustrated by pressure contours and velocity contours, as well as streamlines, which visualize the results of CFD simulations. An AoA of 15º from each Re variation is taken as a sample for the discussion of contours and streamlines. In Figure 6, it can be seen overall that the upper side of the airfoil has lower pressure compared to the lower side of the airfoil, allowing the airfoil to generate lift in accordance with Bernoulli's principle. It is evident that defects in the airfoil can cause higher pressure approximately at the upper side of the airfoil compared to the smooth airfoil. This is of significant concern in terms of the malfunctioning defective airfoil's performance as it can lead to a reduction in C_l. Nevertheless, the pressure distribution in the precincts of the leading edge will also have an impact on changes in C_d caused by the pressure vector in the Y-component.

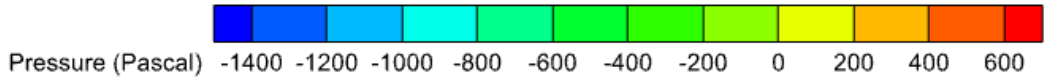

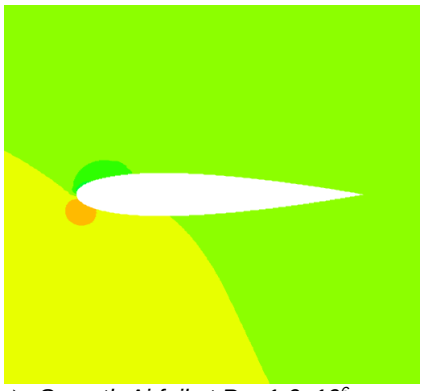

(a) Smooth Airfoil at Re=1.6×10^6

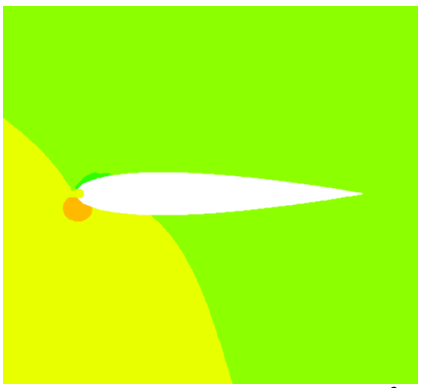

(b) Defect Airfoil at Re=1.6×10^6

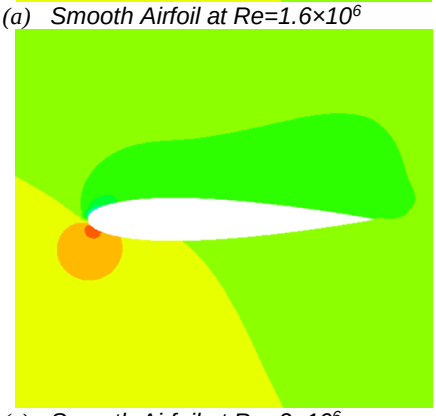

(c) Smooth Airfoil at Re=2×10^6

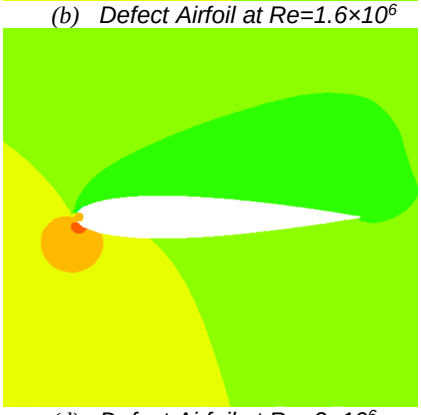

(d) Defect Airfoil at Re=2×10^6

(e) Smooth Airfoil at Re=2.5×10^6

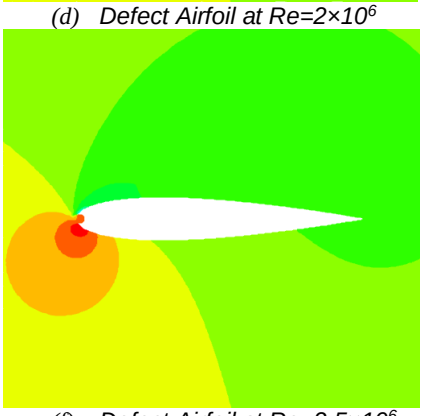

(f) Defect Airfoil at Re=2.5×10^6

Figure 6. Pressure Contours

It can be observed in Figure 7 that all Re variations show the presence of airflow entering the defect region and forming a vortex that prevents the exchange of momentum between the external flow and the flow inside the defect zone also can be called as the cavity of the defect at the leading edge. This results in the surface inside the defect region not being able to interact with the ambient flow, leading to an increase in C_d. As for the vortex formed at the trailing edge of the defective airfoil, it appears larger when stack up with the smooth airfoil. However, there is no significant difference in the vortex at the trailing edge between the defective airfoil and the smooth airfoil when comparing across Re variations.

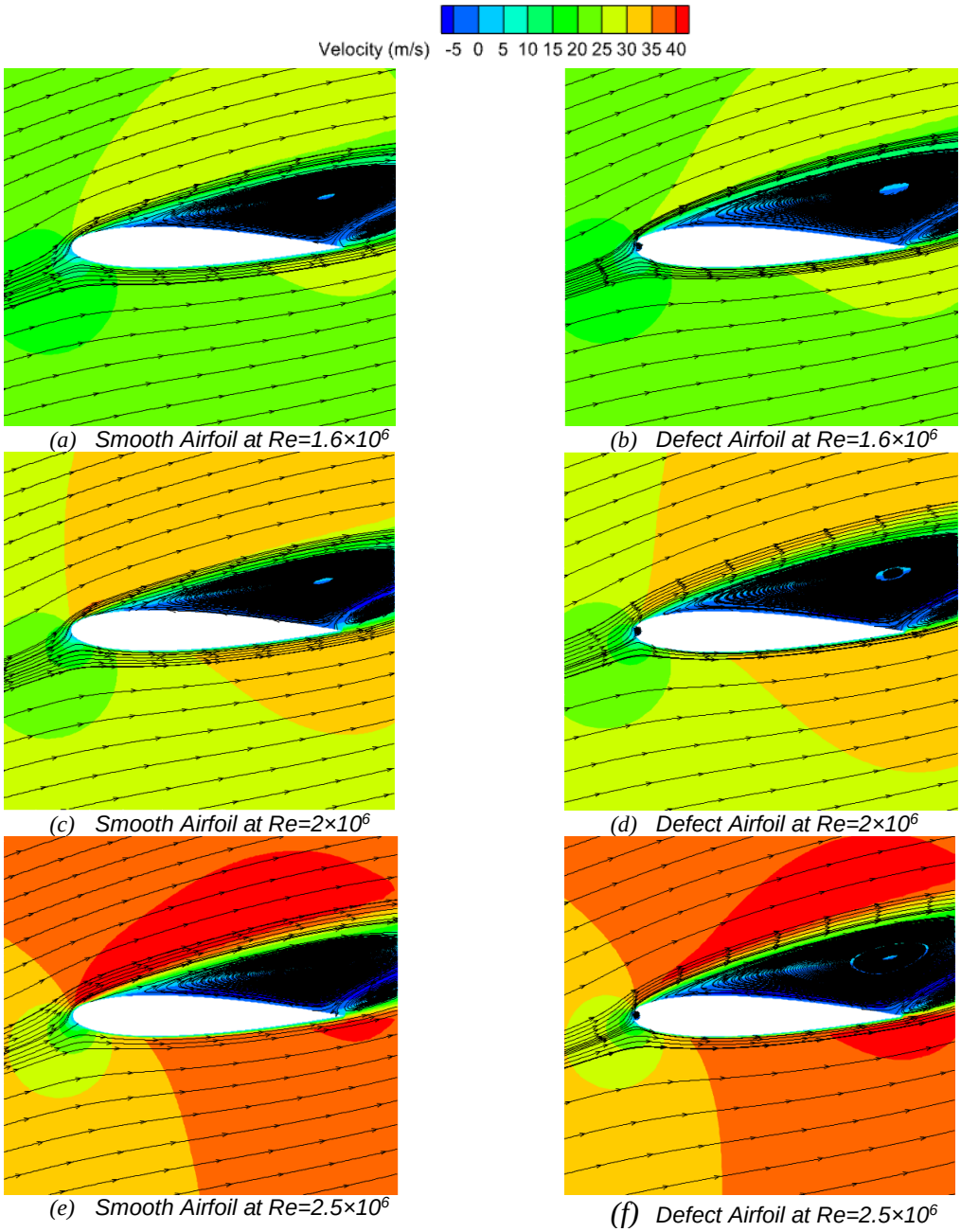

(a) Smooth Airfoil at Re=1.6×10⁶ *(b) Defect Airfoil at Re=1.6×10⁶*

(c) Smooth Airfoil at Re=2×10⁶ *(d) Defect Airfoil at Re=2×10⁶*

(e) Smooth Airfoil at Re=2.5×10⁶ *(f) Defect Airfoil at Re=2.5×10⁶*

Figure 7. Velocity Contours and Streamlines

4. CONCLUSION

In this research, an analysis was conducted on the NACA 0015 airfoil with both smooth and defective configurations. Simulations were performed with three different Re variations, namely 1.6×10^6, 2×10^6, and 2.5×10^6, representing changes in flow velocity. Overall, C_l and C_d increased with increasing AoA for both the smooth and defective airfoils across all Re variations. However, the airfoil would experience stall conditions or a decrease in C_l at an AoA of 9º for the defective airfoil and 11º for the smooth airfoil. The highest C_l value was obtained by the smooth airfoil at $Re=2.5\times10^6$, while the highest C_d value was obtained by the defective airfoil at $Re=2.5\times10^6$. The effective AoA had a maximum C_l at 8º for the defective airfoil, while for the smooth airfoil, it was 10º across all Re variations. The presence of defects in the airfoil resulted in a decrease in C_l and an increase in C_d, leading to a reduction in the C_l/C_d ratio. On average, there was a 44% decrease in C_l at $Re=1.6\times10^6$ compared to the smooth airfoil. Furthermore, at $Re=2\times10^6$ and $Re=2.5\times10^6$, there was a 47% average decrease in C_l values across all angles of

attack. The average increase in C_d values at each AoA was 19% at Re=1.6×10^6, 24% at Re=2×10^6, and 23% at Re=2.5×10^6. The maximum C_l/C_d ratio was achieved at an AoA of 5º for the smooth airfoil at each Re variation, while for the defective airfoil, it reached the maximum C_l/C_d ratio at angles of attack of 6º, 4º, and 5º respectively for Re=1.6×10^6, Re=2×10^6, and Re=2.5×10^6. Additionally, the average decrease in the C_l/C_d ratio at each AoA for all Re variations was 33%. With reference from the analysis of pressure contours, the upper side of the airfoil exhibited lower pressure compared to the lower side for both the defective and smooth airfoils at each Re variation. Defects in the airfoil led to higher pressure alongside the leading edge of the airfoil compared to the smooth airfoil, significantly affecting the decrease in C_l for airfoils with defects. Based on streamline and contour velocity analysis, the vortex formed at the trailing edge of the defective airfoil appeared larger compared to the smooth airfoil. However, there was no difference in the trailing edge vortex when comparing across Re variations. In the case of the defective airfoil, a vortex also formed in the defect region at the leading edge of the airfoil, leading to a significant increase in C_d for airfoils with defects.

REFERENCES

1. Kumar Y, Ringenberg J, Depuru SS, Devabhaktuni VK, Lee JW, Nikolaidis E, et al. Wind energy: Trends and enabling technologies. Vol. 53, Renewable and Sustainable Energy Reviews. Elsevier Ltd; 2016. p. 209–24.
2. Zhang S, Dam-Johansen K, Nørkjær S, Bernad PL, Kiil S. Erosion of wind turbine blade coatings - Design and analysis of jet-based laboratory equipment for performance evaluation. Prog Org Coat. 2015 Jan 1;78:103–15.
3. Conan B, van Beeck J, Aubrun S. Sand erosion technique applied to wind resource assessment. Journal of Wind Engineering and Industrial Aerodynamics. 2012;104–106:322–9.
4. Wang Y, Hu R, Zheng X. Aerodynamic Analysis of an Airfoil With Leading Edge Pitting Erosion. Journal of Solar Energy Engineering, Transactions of the ASME. 2017 Dec 1;139(6).
5. Ge M, Zhang H, Wu Y, Li Y. Effects of leading edge defects on aerodynamic performance of the S809 airfoil. Energy Convers Manag. 2019 Sep 1;195:466–79.
6. Wang Y, Zheng X, Hu R, Wang P. Effects of leading edge defect on the aerodynamic and flow characteristics of an s809 Airfoil. PLoS One. 2016 Sep 1;11(9).
7. Sareen A, Sapre CA, Selig MS. Effects of leading edge erosion on wind turbine blade performance. Wind Energy. 2014;17(10):1531–42.
8. Gad-El-Hak M. Reynolds number effects in wall-bounded turbulent flows [Internet]. 1994. Available from: http://appliedmechanicsreviews.asmedigitalcollection.asme.org/
9. Lissaman PBS. LOW-REYNOLDS-NUMBER AIRFOILS [Internet]. Vol. 15, Ann. Rev. Fluid Mech. 1983. Available from: www.annualreviews.org
10. Islam Rubel R, Uddin K, Islam Z. Numerical and Experimental Investigation of Aerodynamics Characteristics of NACA 0015 Aerofoil. Vol. 2, INTERNATIONAL JOURNAL of ENGINEERING TECHNOLOGIES Robiul Islam Rubel et al. 2016.
11. Julian J, Iskandar W, Wahyuni F. COMPUTATIONAL FLUID DYNAMICS ANALYSIS BASED ON THE FLUID FLOW SEPARATION POINT ON THE UPPER SIDE OF THE NACA 0015 AIRFOIL WITH THE COEFFICIENT OF FRICTION. Jurnal Media Mesin. 23(2).
12. Seeni AS, Rajendran P. Numerical validation of NACA 0009 airfoil in ultra-low reynolds number flows. International Review of Aerospace Engineering. 2019;12(2):83–92.
13. Iskandar W, Julian J, Wahyuni F, Ferdyanto, Prabu HK, Yulia F. Study of Airfoil Characteristics on NACA 4415 with Reynolds Number Variations. International Review on Modelling and Simulations. 2022;15(3):162–71.
14. Megawanto FC, Harinaldi, Budiarso, Julian J. Numerical analysis of plasma actuator for drag reduction and lift enhancement on NACA 4415 airfoil. In: AIP Conference Proceedings. American Institute of Physics Inc.; 2018.
15. Minh Triet N, Ngoc Viet N, Manh Thang P. Aerodynamic Analysis of Aircraft Wing. Vol. 31, VNU Journal of Science: Mathematics-Physics. 2015.
16. Gharali K, Johnson DA. Numerical modeling of an S809 airfoil under dynamic stall, erosion and high reduced frequencies. Appl Energy. 2012;93:45–52.
17. Kekina P, Suvanjumrat C. A Comparative Study on Turbulence Models for Simulation of Flow Past NACA 0015 Airfoil Using OpenFOAM.